Global maps of anhydrous minerals at the surface of Mars from OMEGA/MEx

A. Ody,[1] F. Poulet,[1] Y. Langevin,[1] J.-P. Bibring,[1] G. Bellucci,[2] F. Altieri,[2] B. Gondet,[1] M. Vincendon,[1] J. Carter,[3] and N. Manaud[4]

Received 2 May 2012; revised 1 August 2012; accepted 6 August 2012; published 20 September 2012.

[1] We here reassess the global distribution of several key mineral species using the entire OMEGA/Mars Express VIS-NIR imaging spectrometer data set, acquired from orbit insertion in January 2004 to August 2010. Thirty-two pixels per degree global maps of ferric oxides, pyroxenes and olivines have been derived. A significant filtering process was applied in order to exclude data acquired with unfavorable observation geometries or partial surface coverage with water and CO_2 frosts. Because of strong atmospheric variations over the 3.6 Martian years of observations primarily due to the interannual variability of the aerosol opacity, a new filter based on the atmospheric dust opacity calibrated by the Mars Exploration Rovers measurements has also been implemented. The Fe^{3+} absorption features are present everywhere on the surface, with a variety of intensities indicating distinct formation processes. The pyroxene-bearing regions are localized in low albedo regions, while the bright regions are spectrally comparable to anhydrous nanophase ferric oxides. The expanded data set increases by a factor of about 2, the number of olivine detections reported in previous OMEGA-based studies. Olivine is mainly detected in three types of areas over the Martian surface: discontinuous patches on the terraces of the three main basins; smooth inter-crater plains and smooth crater floors throughout the southern highlands; and crater sand dunes, crater ejectas and extended bedrock exposures in the northern plains. Olivine is also detected in the low albedo pyroxene-bearing dunes surrounding the northern polar cap.

Citation: Ody, A., F. Poulet, Y. Langevin, J.-P. Bibring, G. Bellucci, F. Altieri, B. Gondet, M. Vincendon, J. Carter, and N. Manaud (2012), Global maps of anhydrous minerals at the surface of Mars from OMEGA/MEx, *J. Geophys. Res.*, *117*, E00J14, doi:10.1029/2012JE004117.

1. Introduction

[2] The surface composition of Mars records the past and present geologic and climatic processes of the planet. In situ analyses performed by landers and rovers over the last few decades have provided unique analyses of rocks and minerals. However, these in situ investigations constitute a small and non-random sampling of the Martian surface, while orbital remote sensing observations enable a global characterization of Mars surface properties.

[3] During the past fifteen years, the Mars orbiters have provided great strides in our understanding of the composition and of the physical properties of the surface of Mars [e.g., *Bell*, 2008]. The visible near-infrared imaging spectrometer OMEGA (Observatoire pour la Minéralogie, l'Eau, les Glaces et l'Activité) on board the ESA Mars Express (MEx) mission is one among the numerous remote sensing instruments that contributes to these achievements. The nearly polar, highly eccentric orbit of Mars Express provides a variable spatial sampling which, together with a latitude drift of the periapsis enables a complete coverage at different spatial scales. This made it possible for OMEGA to achieve almost global km-scale coverage of the Martian surface.

[4] Based on the first Martian year of OMEGA operations, a first analysis of the global distribution of key mineral species at low and midlatitudes was performed, using the 1–2.5 μm wavelength range [*Poulet et al.*, 2007]. This analysis, using spectral parameters, revealed general trends of the distribution of surface material on Mars, broadly consistent with previous ground-based [e.g., *McCord et al.*, 1982] and space observations [e.g., *Bandfield*, 2002]. Low NIR 1 μm albedo (<0.2) regions exhibit pyroxene signatures, while the bright regions (NIR 1 μm albedo >0.3) are interpreted as being covered by anhydrous ferric oxides. Olivine has been identified in large areas associated with low albedo pyroxene-bearing highlands with a predominant Mg-rich composition and a grain size distribution smaller than 100 μm. Olivine with higher iron content and/or larger grain size

[1]IAS, Université Paris-Sud, Orsay, France.
[2]Istituto di Astrofisica e Planetologia Spaziali, INAF, Rome, Italy.
[3]European Southern Observatory, Santiago, Chile.
[4]European Space Astronomy Center, Villanueva de la Cañada, Spain.

Corresponding author: A. Ody, IAS, Université Paris-Sud, FR-91405 Orsay CEDEX, France. (anouck.ody@ias.u-psud.fr)

0148-0227/12/2012JE004117

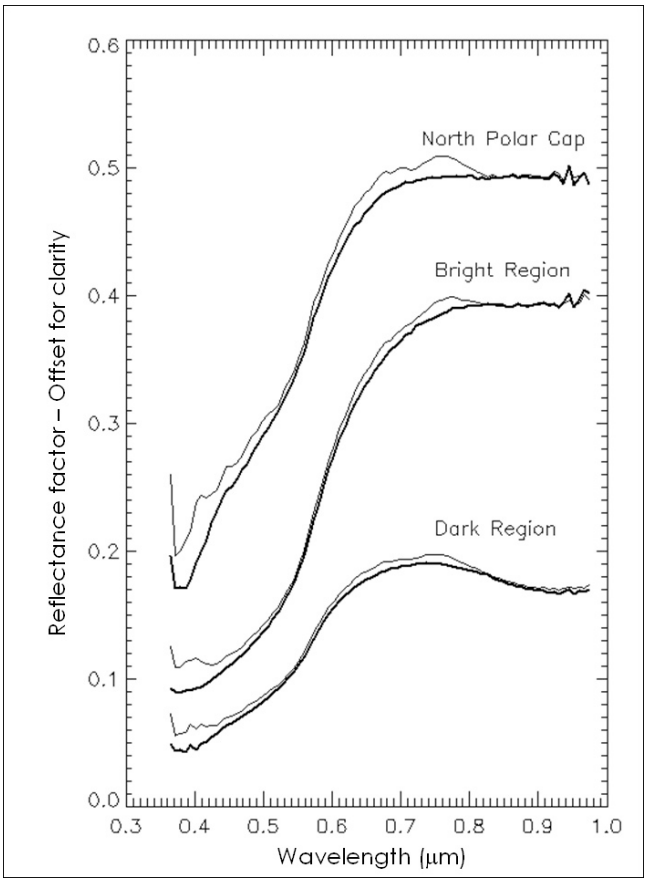

Figure 1. Comparison between VIS spectra (<1 μm) before (thin gray line) and after (thick black line) the improvement of the Instrumental Transfer Function and internal stray light correction procedure for the VIS channel.

(>100 μm) is detected in isolated areas. The spectral properties of the low albedo terrains in the northern plains were interpreted as resulting from a thin ferric coating or varnish present on dark basaltic substrate. Finally, hydrated minerals have been detected in spots, mostly within the ancient crust as also confirmed by further studies [*Poulet et al.*, 2007, 2009a; J. Carter et al., Hydrous minerals on Mars as seen by the CRISM and OMEGA imaging spectrometers: Updated global view, submitted to *Journal of Geophysical Research*, 2012].

[5] OMEGA-based distributions of anhydrous mineral species at high latitudes (>50°) have been mapped using data acquired during the northern and southern springs and summers of the first two Martian years [*Poulet et al.*, 2008]. Mafic materials (both pyroxene and olivine) were found in low albedo terrains, while the presence of hydrated minerals is reported at latitudes higher than 60°.

[6] The goal of this paper is to reassess the global distribution of these mineral species at low, middle and high latitudes using the entire OMEGA data set acquired from orbit insertion in January 2004 to the failure of the 1–2.5 μm channel cooler, in August 2010. The two OMEGA coolers were rated for the nominal mission (1 Martian year). They greatly exceeded these expectations, and the cooler of the 2.5–5.1 μm channel is still operating nominally. The 1–2.5 μm channel provided important discriminating criteria for the Martian mineralogy, hence the maps presented in this paper can be considered as a finalized outcome of OMEGA observations.

[7] We address four key compositional aspects: pyroxene, olivine, ferric phases, nanophase oxides, which are mapped using diagnostic mineral parameters. Such a fast mapping technique has the advantage of being well-adapted to the large OMEGA data set. Section 2 describes the status of the OMEGA instrument as a function of its aging and the selection of the data set used for the mapping. Section 3 presents the key mineral indicator parameters used in this study. Results are then presented and discussed in section 4. We will see that these new global maps are in good agreement with the major trends of mineral distributions reported in *Poulet et al.* [2007, 2008]. In addition, the new maps are much more complete than the previous ones, and they will be used as high level data sets to identify regions of interest and to perform detailed local analyses at resolution of hundreds of meters. Such science application on the olivine distribution will be presented in a forthcoming paper (A. Ody et al., Global investigation of olivine on Mars: Insights into crust and mantle compositions, submitted to *Journal of Geophysical Research*, 2012).

2. Data Products and Methods

[8] The OMEGA spectral range extends from the visible (0.36 μm) to the thermal infrared (5.09 μm). (All OMEGA data, the data reduction updated software and complementary information are available on the ESA PSA website (http://www.rssd.esa.int/index.php?project=PSA) [*Heather et al.*, 2010].) The present analysis focuses on VNIR reflectance measurements (0.36–2.5 μm) using the VIS (0.36–1.07 μm) channel [*Bellucci et al.* 2006] and the NIR (0.92–2.7 μm) C-channel [*Bibring et al.*, 2004]. The OMEGA IFOV (Instantaneous Field Of View) is 1.2 mrad (4 arcmin). OMEGA operates with cross track swaths of 16, 32, 64, or 128 IFOV in width, so as to provide consistency between cross-track and along-track sampling as a function of MEx altitude. This translates into a footprint (pixel size) ranging from a few hundred meters (observations close to periapsis) to a few kilometers (from 4000 km altitude).

2.1. VIS Channel: Updated Data Processing

[9] OMEGA operates as a push broom imager in the VIS (the swath is acquired in a single integration over a 2-D detector). In this work, we use an updated version of the data reduction procedure including an improved Instrumental Transfer Function (ITF) and an internal stray light correction. Details on the method to retrieve the updated ITF can be found in F. G. Carrozzo et al. (Study of the 1 micron band spectral properties to characterize the Martian mineralogy by means of the OMEGA/MEX data, submitted to *Journal of Geophysical Research*, 2012). Figure 1 illustrates the benefits of the new calibration. Measurements for wavelengths greater than 0.98 μm (spectral channel 84) must be discarded, since sensitivity drops.

2.2. C-Channel: Instrumental Evolution and Updated Data Processing

[10] The C-channel of OMEGA operated in a whiskbroom mode in which the spectrum was acquired for a single IFOV, 4 × 4 arcmin in size. The image was built using (1) a mirror

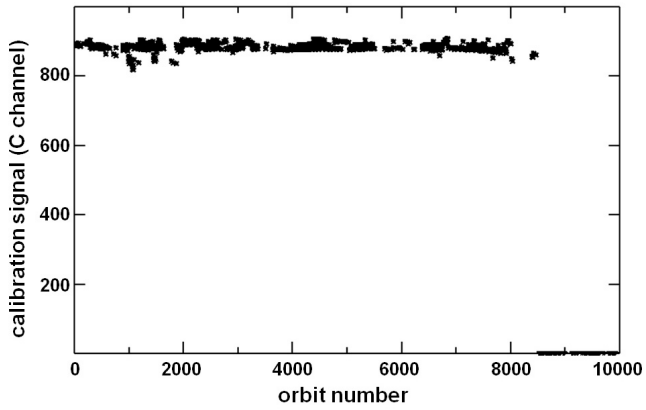

Figure 2. Evolution of the signal of the calibration lamp in the C-channel from orbits 0 to 10000. The black stars correspond to spectel 102 (C-channel, 2.67 μm).

in front of the telescope, which scanned the surface in a crosstrack direction, with swaths of 16, 32, 64 or 128 pixels depending on the spacecraft altitude, thus on its on-ground drift velocity, and (2) the drift of the spacecraft. The swath width was chosen so as to avoid both undersampling and oversampling between swaths. The C-channel image cubes have thus dimensions Npix x Nline x 128, where Npix is 16, 32, 64 or 128, Nline corresponds to the number of scans within the cube, and 128 corresponds to the number of spectral channels (spectels). Because the scanning mirror is flat, we assume that a single photometric response can be applied to all observations, an approach which was verified during ground calibration and validated in-flight [*Bonello et al.*, 2005]. Thermal emission can be neglected for the C-channel, which extends from 0.93 μm to 2.7 μm, by contrast with the L-channel (2.5 to 5.1 μm) [*Jouglet et al.*, 2007].

[11] The C-channel detector was cooled down to ~77°K by a dedicated cryocooler, while the entire spectrometer is cooled to 190°K by a conductive link to a passive radiator. OMEGA's power consumption is 27.4 W during the ~2 h cooling of the focal plane. A slow degradation of the performance of the C-channel cooler began to be observed in 2009. This evolution accelerated in early 2010. Starting in April (orbit 8000), the C-channel operational temperature was reached a few minutes after the previously nominal cooling duration. In late August 2010, the C cooler suddenly displayed a current spike which resulted in an automatic shut-down of OMEGA by the spacecraft. This led to the decision not to turn on this channel for later observations.

[12] The evolution of the OMEGA channels with time has been monitored using an internal calibration lamp. As shown in Figure 2, the level of the signal in the C-channel was very stable from January 2004 (start of operations) to April 2010 (orbit 8000). The initial photometric function remained valid except for hot spectels (see below).

[13] The degradation of the C-channel detector, due to cosmic rays, needs also to be taken into account in the pipeline. The impact of a cosmic ray can indeed result either in a slightly lower photometric efficiency (typically by a factor 0.8 to 0.95, "hot spectels") which remains stable after the event, or in an unstable behavior, observed whenever the efficiency decreases to <0.8 ("dead spectels"). After 6+ years of operation of the C-channel, 95 spectels were still fully nominal (Figure 3), 15 were hot and 18 where declared dead. For hot spectels, the pipeline applies either the initial photometric response or the lower photometric response by comparing the orbit number to the orbit number at which the degradation was observed. Dead spectels are not considered in the interpretation, hence

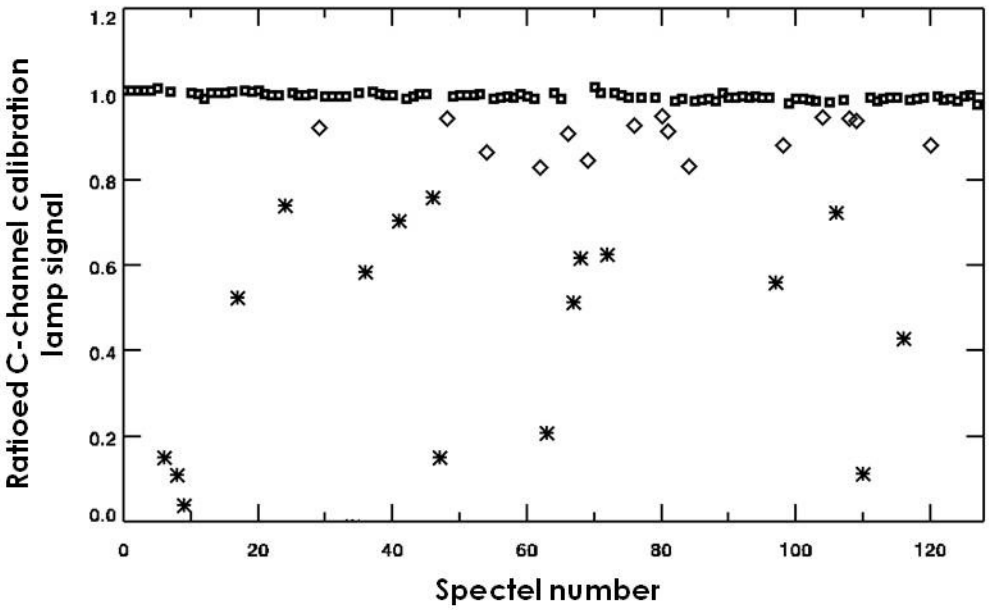

Figure 3. Ratio of the level of the calibration lamp in the C-channel for orbit 7801 (02/2010) to that for orbit 6 (01/2004, start of science operations). After 6 years, 15 spectels have been slightly impacted by cosmic rays (calibration signal lowered by 0.8 to 0.95, diamonds) while 17 spectels have been strongly impacted (calibration signal lowered by more than 0.8, stars).

the pipeline provides an array of useful spectels with a number of elements which decreased from 127 at the start of observations to 110 in early 2010. The spectral signatures of silicates and oxides are broad, so that the degradation of the C-channel detector array by cosmic rays had only a limited impact on the usefulness of late orbits for mapping such minerals.

[14] After 6 months of fully nominal operations, a perturbation appeared for pixels 80 to 95 of the 128 pixels large swaths, with spurious values for 4 spectels every 32 spectels across the 3 spectral channels. Only the valid regions (pixels 0:79, 96:127) have been considered for map building. In April 2008, the perturbations extended first to the full second half of 128 pixel swaths, then to the whole swath. After investigating the problem, the OMEGA team decided in June 2008 to switch on the redundant main electronics, which made it possible to resume nominal operations. However, due to the anomalous behavior of the scanner when cold, most observations after June 2008 where implemented using the 16, 32 or 64 pixel swaths only.

2.3. Filtering the Data

2.3.1. Processes

[15] Global maps of key Martian minerals are built using the full OMEGA data set acquired from January 2004 (in-orbit commissioning) to August 2010 (loss of the C-channel cooler). This data set corresponds to 3.6 Martian years of observations, 2047 OMEGA operating orbits (over 8485 MEx orbits), 9618 3D image-cubes and more than 700 million pixels. The VNIR radiance data are converted to reflectance using the observational constraints and a solar spectrum scaled to the Mars-Sun distance. A near-infrared atmospheric correction is applied between 1 μm and 2.6 μm by assuming that the atmospheric contribution follows a power law variation with altitude [*Langevin et al.*, 2007]. This produces a corrected reflectance (I/Fcos(i))(λ) spectrum which corresponds to the ratio of the observed radiance to the incoming solar flux per unit of surface assuming a lambertian surface.

[16] Various instrumental and observational effects affect the quality of the data and hence the mapping of the minerals. The data are thus filtered according to three major steps in order to keep only relevant data for mapping the mineral species:

[17] 1. The first step consists of excluding data cubes on the basis of coverage and operation modes criteria. The high spatial resolution observations with a swath width of 16 pixels are not used because their tracks are too narrow ($\sim$6 km) to contribute significantly to the global mapping (mode 16 on Figure 4a). Then, only data cubes acquired in near-nadir pointing mode (emergence angle <15°) and during day time (incidence angle <90°) have been considered. Third, because we need the near-IR to assess the presence of CO_2 or water frosts and ices (see section 3), observations made only with the visible channel are removed from the data set. Finally, we removed data cubes acquired before OMEGA had reached its nominal operation start time, as these acquisitions were performed to heat up the instrument, and primarily its scanner, before it scans in 128 pixels swaths for which a minimum temperature was required (heating cubes in Figure 4a). Note that most of these data were acquired before the IR detectors reached their nominal operating temperature. Figure 4a summarizes the number of OMEGA data cubes filtered by each of these conditions. Most of the data cubes have been removed because of the "16" cross track swath or non-Nadir conditions. After this first filtering, our data set is composed of 6653 data cubes, which correspond to 56% of the initial data set in terms of number of pixel (>400 million pixels).

[18] 2. A second filtering step was applied to data cubes pixels that exhibit anomalies. These result either from the saturation of the C-channel, a non-nominal NIR detector temperature, electronic deficiencies (degradation of the Main Electronics (ME) in Figure 4b) or telemetry problems (data gaps on Figure 4b). Each part of the cubes affected by one or more of these four anomalies was excluded. This step removed about 9.6% of the pixels for the NIR and only 5.5% for the VIS (Figure 4b). In addition, the calibration data (first scans of the first cube of each orbit for the IR and first scans of each data cube for the visible part) were removed (green portion on Figure 4b). These two additional steps removed about 0.5% pixels in the IR range and 1.7% in the visible range (green in Figure 4b).

[19] 3. Observational conditions (optical thickness of aerosols, air mass, altitude, clouds, surface icy frost) are critical for the mapping of surface mineral species. At high incidence angles, the contribution of aerosol scattering hampers identifying mineralogical signatures. The useful data set was therefore restricted to pixels observed with an incidence <75° (w.r.t the outward normal to the reference ellipsoid). Even at relatively low incidence, observations taken during periods of high aerosol optical thickness cannot be fully exploited for mineralogical identifications (aerosols in Figure 4c). An additional aerosol criterion was thus applied as detailed below (section 2.3.3). Finally, seasonal surface frosts (H_2O or CO_2) and/or ice clouds (mainly H_2O) exhibit strong spectral signatures in the NIR, which mask mineralogical features. Data cubes presenting such features according to a procedure detailed in section 2.3.2 have been also excluded. As illustrated in Figure 4c, observation conditions (incidence, aerosol optical thickness and ices) are responsible for the removal of $\sim$54% of pixels within the 6653 image cubes previously selected after step (1).

[20] After completing these filtering procedures, $\sim$23.2% of the initial 9618 OMEGA cubes (170 million pixels) have been processed and mapped in the NIR range and $\sim$23.9% in the VIS range.

2.3.2. Water and CO_2 Ices and Frosts

[21] Water and CO_2 ices are commonly present on Mars in the form of clouds and seasonal frosts. Both have an absorption band centered at about 1.5 μm, which can bias the detection of pyroxene and olivine and affect the signatures of the ferric phases. Therefore we decided to disregard all spectra in which either H_2O ice, identified by its 1.5 μm absorption band, or CO_2 ice identified by its 1.43 μm absorption band is present. The water and CO_2 ice criteria as defined in *Langevin et al.* [2007] were modified, for orbit greater than 7768 and 4330 respectively, because of the failure of several spectels (Table 2). In order to remove disturbed data without losing to much data coverage, we fixed the detection threshold of the CO_2 ice spectral parameter to 5% and that of H_2O to 3%.To minimize the effects of seasonal frosts in the polar regions, we applied an

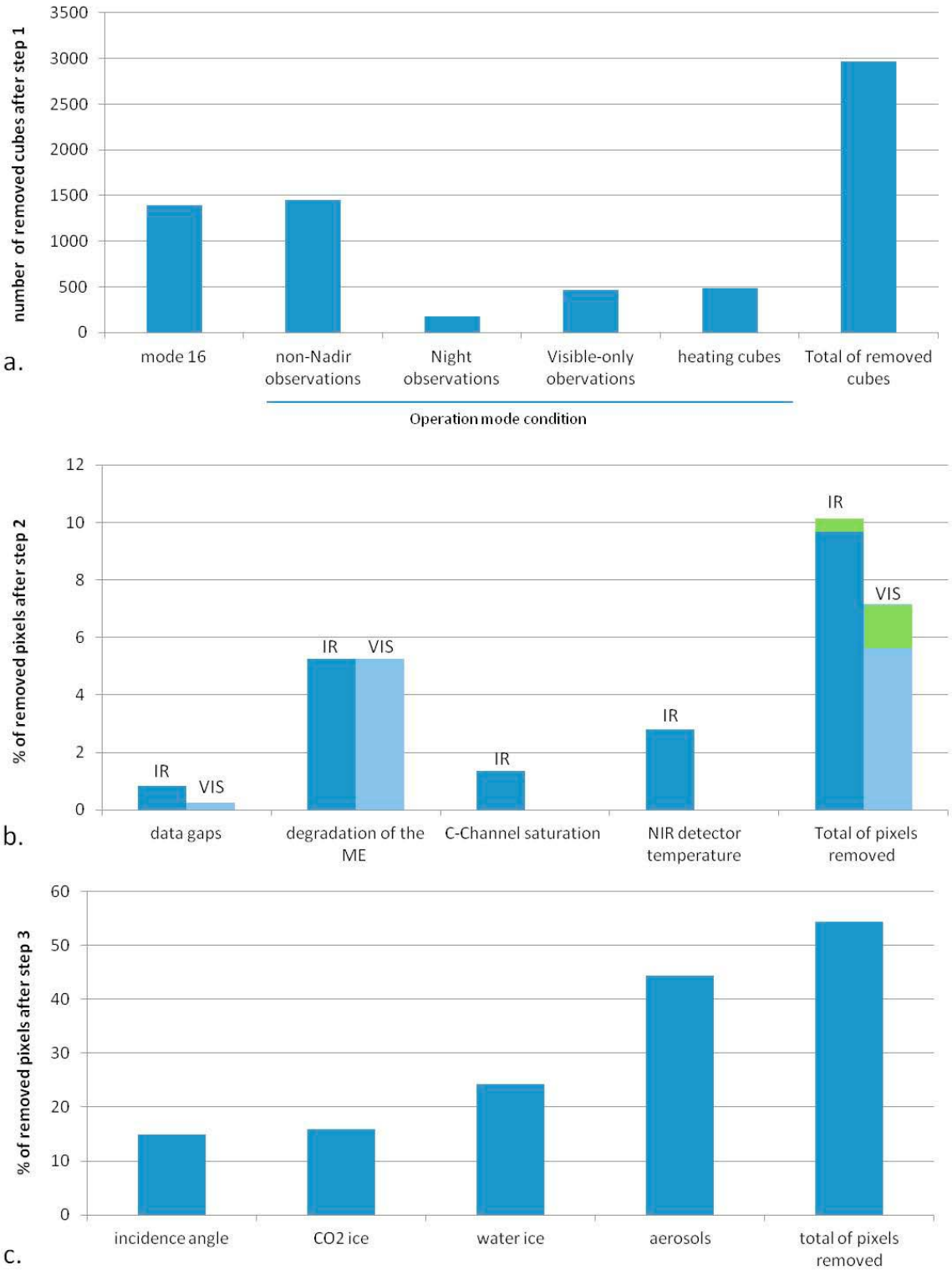

Figure 4. (a) Histogram of the data cubes filtered by coverage, operation mode and data quality (step 1 in text). (b) Histogram of the percentage of pixels removed after step 2 due to instrumental anomalies (blue portions) or because they correspond to calibration data (green portion), with respect to the total number of pixels in the 6653 cubes extracted from step 1. (c) Histogram of the percentage of pixels removed by various filters based on observational conditions (presence of ices and aerosols) (step 3 in text), with respect to the total number of pixels in the 6653 cubes extracted from step 1. The total number of removed pixels does not correspond to the sum of the pixels removed by each condition, as some pixels can meet several rejection conditions simultaneously.

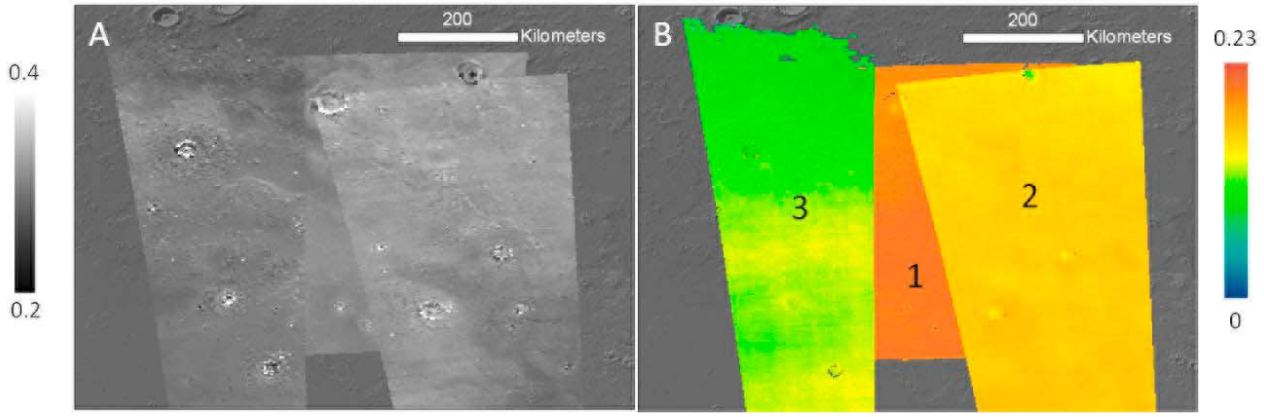

Figure 5. Three OMEGA tracks ((a) NIR albedo; (b) Fe^{3+} parameter) over the regions of coordinates [114–128°E; 32–43°N] taken at different seasons and years (Table 1). Numbers correspond to cube numbers in Table 1.

additional solar longitude constraint to latitudes poleward of 50°N and 50°S restricting data to local spring and summer acquisitions, namely to Ls = [45°–160°] for the northern regions and to Ls = [220°–330°] for the southern ones.

2.3.3. Aerosol-Based Filtering Process

[22] Observations acquired over different seasons and years shows variations of the values of spectral parameters. They result from both annual and interannual variability of the atmospheric dust opacity [*Vincendon et al.*, 2007, 2009]. The 2007 global maps were less affected by these effects, because they were based on data acquired during the first Martian year of OMEGA observations (2004–2006) only. Our objective being to produce "aerosol-free" surface maps, the contribution of aerosol scattering has been assessed and removed, using the Monte-Carlo modeling approach presented in *Vincendon et al.* [2009] and *Vincendon and Langevin* [2010]. However, such an approach cannot be applied to the whole data set given the computing time required. Therefore, we followed a filtering approach to restrict the data set to optical thicknesses along the path for which aerosol contributions do not hamper mineral identifications.

[23] Two filtering steps were applied before mapping the spectral parameters. First, observations acquired during the global high opacity dust storm of 2007 that occurred between Ls 260° and Ls 325°, were removed. However, significant variations of the dust opacity with time still impact the mosaics. This is illustrated in Figure 5a that shows the overlap of three OMEGA tracks of the Fe^{3+} parameter (see section 3.4) taken at three different years and solar longitudes. Average values of the Fe^{3+} spectral parameter and observations conditions for these three cubes are reported in Table 1. Cube 1 is extracted from observations acquired during clear atmospheric conditions (Ls ~ 20°–130°) and presents a high average Fe^{3+} spectral parameter value of about 0.20. The other two cubes (2 and 3) acquired during a dusty period exhibit an increased reflectance at short wavelength (0.4–0.6 μm) which results in a decrease in the Fe^{3+} signature (Table 1).

[24] The strongest spectral and quantitative effects of aerosols are observed in the visible wavelength range due to their effective grain size radius of about 1.5 μm and their spectral properties [*Vincendon et al.*, 2007]. The Fe^{3+} spectral parameter is the most sensitive to variations in dust opacity. This spectral parameter is then used as a proxy of data affected by atmospheric dust. In order to derive a rejection threshold based on the dust opacity, we calculated the values of the Fe^{3+} criterion for typical low and high albedo regions, and then correlated these values with the dust opacity for all data cubes acquired over these regions at different seasons and years. The dust opacity has been measured by the Panoramic Camera (Pancam) on both Mars Exploration Rovers (MERs) at 0.9 μm [*Lemmon et al.*, 2004; M. T. Lemmon, private communication, 2009]. *Vincendon et al.* [2009] have demonstrated that the dust optical depth is relatively homogeneous over low and middle latitudes and nearly independent of the longitude for a given epoch. Therefore, the MER-based dust opacity can be considered as a good proxy of the dust opacity for the latitudes [−60°, +60°]. It can be noted that the optical depths of the two rovers are interpolated at each solar longitude. The mean evaluated optical depth was then extrapolated to the actual incidence (with respect to the reference ellipsoid) and altitude of each OMEGA pixel (Table 2).

[25] Figure 6 shows the correlation between the averaged values of the Fe^{3+} spectral parameter calculated for each studied data cube and the dust optical depth over bright and dark regions of Mars. The value of this spectral parameter

Table 1. Observation Conditions and Average Values of the Fe^{3+} Spectral Parameter for the Three Spectra Cubes Shown in Figure 5

Cube Number	OMEGA Data Cube	Ls	Terrestrial Years	Incidence Angle	Effective Dust Opacity	Average Fe^{3+} Value
1	ORB0329_4	23°	2004	33°	1.59	0.20
2	ORB6544_5	205°	2009	52°	2.60	0.16
3	ORB4411_5	256°	2007	64°	3.97	0.11

Table 2. Spectral Parameter Used in the Filtering Process[a]

Name	Formulation	Detection Threshold	Rationale
Water ice	$R(1.50)/(R(1.39)^{0.7}*R(1.77)^{0.3})$ before orbit 7768 $(R(1.53)/(R(1.39)^{0.63}*R(1.77)^{0.37}))*1.04–0.02$ after orbit 7768[b]	0.97	1.5 μm due to water ice
CO_2 ice	$1-R(1.43)/(R(1.39)^{0.5}*R(1.44)^{0.5})$ before orbit 4330 $1-R(1.43)/R(1.39)$ after orbit 4330[c]	0.05	1.43 μm due to CO_2 ice
Dust opacity rejection criterion	$\tau_{MERs}*\exp(alt/H)*(1 + 1/\cos(i))$ with H (11 kms) the Martian scale height and i the incidence angle relative to the reference ellipsoid.	2	Effective dust opacity measured by the MERs at 0.9 μm corrected from altitude and incidence angle.

[a]R is the reflectance I/F at a given wavelength λ (μm)/cos(i) with i as incidence angle relative to the local normal.
[b]Spectel 40 (1.50 μm) became non-functional after orbit 7768 due to cosmic ray degradation. After this orbit, spectel 40 (1.50 μm) was replaced by spectel 42 (1.53 μm) and water ice spectral parameter was modified so as to be consistent with the first spectral parameter threshold.
[c]Spectel 36 (1.44 μm) became non-functional after orbit 4330 due to cosmic ray degradation. The criterion used before the loss of this spectel was less sensitive to altitude, as this narrow CO_2 band centered at 1.43 μm partly overlaps with an atmospheric CO_2 band.

decreases as the optical depth increases for both bright and dark regions. This decrease is especially strong for dust opacity >1.5–2. A decrease of more than 25% is observed when the dust optical depth is ~2.5. This decrease can reach 50% for an optical depth of 4.

[26] A threshold of the dust rejection criterion for values between 1.8 and 2.2 was tested on the dust-disturbed Fe^{3+} global map and it appears that a threshold of 2.0 is the best trade-off between removal of most of the dust-contaminated data and keeping valuable data and spatial coverage. The other spectral parameters are less sensitive to aerosols but because the global coverage is not much affected by this rejection criterion, we decided, in order to remain consistent, to apply a dust opacity threshold at 2 on all global maps. As expected, the opacity-based filtering technique was not effective for the high latitudes, and it was not applied on northern and southern polar maps.

3. Spectral Parameters of Mapped Minerals

[27] This section presents the set of diagnostic mineral parameters that capture key mineralogical properties of the surface. These parameters, which were first developed in *Poulet et al.* [2007], were adapted to take into account the aging of the C-channel detector and the new calibration

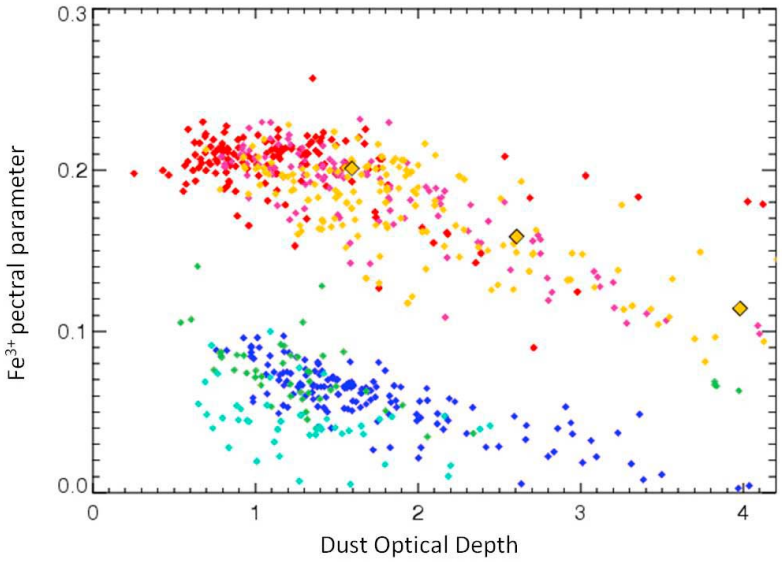

Figure 6. Evolution of the Fe^{3+} spectral parameter as a function of the incidence-altitude corrected dust opacity at 0.9 μm measured by the MER/PanCam instrument [*Lemmon et al.*, 2004; Lemmon, private communication, 2009] for selected bright regions (warmer colors) and dark regions (cooler colors). Each point represents the average value of the Fe^{3+} spectral parameter versus the average value of dust opacity calculated for cubes extracted from various regions: Tharsis terrain [235°,277°E; 4°,26°N], Arabia Terra terrain [8°,41°E; 12°,31°N] and two Elysium terrains [100°,118°E; 13°,38°N and 140°,174°E; 3°,30°N] for bright regions and the north of Argyre basin [302°,343°E; −28°,−8°N], Syrtis Major terrain [67°,77°E; 1°,19°N] and Tyrrhena Terra terrain [79°,101°E; −25°,−9°N] for dark regions. Large yellow diamonds outlined in black represent values for the three spectral cubes of Figure 5.

Table 3. Description of Mapped Spectral Parameters[a]

Name	Formulation	Detection Threshold	Rationale
NIR albedo	R(1.08)	N/A	Lambertian albedo
0.53 μm band depth or Fe^{3+} parameter	1-R(0.55)/(0.5*R(0.44) + 0.5*R(0.65))	0	Degree of oxidation of the surface
Nanophase ferric oxide or 1/0.8 μm slope	R(0.88)/R(0.78)	1	Nanophase ferric oxide if ratio≥1
Pyroxene	1-(R(2.15) + R(2.22))/(R(1.79) + R(2.5))	0.01	2 μm band due to both high-calcium and low-calcium pyroxene
OSP1 (Olivine Spectral Parameter 1)	(0.5*R(1.54) + 0.5*R(1.56))/(0.1*R(1.01) + 0.2*R(1.21) + 0.7*R(1.36)) before orbit 7768 (0.5*R(1.54) + 0.5*R(1.56))/(0.1*R(1.03) + 0.2*R(1.21) + 0.7*R(1.36)) after orbit 7768[b]	1.04	1 μm band due to olivine with low iron content and/or small grain size and/or low abundance
OSP2 (Olivine Spectral parameter 2)	(0.5*R(1.69) + 0.5*R(1.70))/(0.05*R(1.01) + 0.05*R(1.21) + 0.45*R(1.36) + 0.45*R(1.5) before orbit 7768 (0.5*R(1.69) + 0.5*R(1.70))/(0.05*R(1.03) + 0.05*R(1.21) + 0.45*R(1.36) + 0.45*R(1.48) after orbit 7768[b]	1.04	1 μm band due to olivine with higher iron content and/or larger grain size and/or higher abundance
OSP3 (Olivine Spectral parameter 3)	$R(1.36)/(R(1.07)^{0.5}*R(1.64))^{0.5}$	Median (OSP3)-0.04	1 μm band due to olivine with higher iron content and/or larger grain size and/or higher abundance

[a]R is the reflectance I/F at a given wavelength λ (μm)/cos(i) with i as incidence angle relative to the local normal.
[b]Spectel 6 (1.01 μm) and spectel 40 (1.5 μm) became non-functional after orbit 7768 due to cosmic ray degradations. They have been replaced by spectels 7 (1.03 μm) and 39 (1.49 μm) for evaluating OSP1 and OSP2 after this orbit.

procedure of the visible channel. All these parameters are listed in Table 3.

3.1. NIR 1 μm Albedo

[28] A NIR 1 μm albedo map was produced using the I/F/cos(i) value at 1.08 μm (with i the solar incidence angle), assuming a lambertian surface. The 1.08 μm wavelength was here selected to enhance the contrast between mafic regions, which show strong absorption bands at 1 μm due to the presence of pyroxene and olivine minerals, and non-mafic regions. The resulting NIR albedo map can be used as a reference to maps built with the other spectral parameters listed in Table 1 and described hereafter.

3.2. Pyroxene

[29] The pyroxene spectral parameter is based on its 2 μm absorption band attributed to crystal field transitions in Fe^{2+} when occupies the M2 crystallographic site instead of Ca^{2+}. Although this band shifts to higher wavelengths with increasing Ca^{2+}, this parameter is defined to be sensitive to both low- and high-calcium pyroxene. Two spectels have been changed with respect to the 2007 spectral parameter because of the aging of the detector. These small changes do not affect the threshold of 1% derived by *Poulet et al.* [2007].

3.3. Olivine

[30] The identification of olivine is based on its broad 1 μm band due to Fe^{2+} ion in distorted octahedral sites. This complex absorption band varies in width, position, and shape with the iron content of the olivine but also with its grain size and its abundance. The right wing of the absorption band shifts toward longer wavelengths as the FeO content in the olivine increases. However, an increase in the grain size broadens the bottom of the band and also shifts the right wing of the band toward longer wavelengths. Thus, a forsterite olivine spectrum with very large grains ($\gg$100 μm) and a fayalite olivine spectrum with smaller grains have similar spectral features. In addition, the eventual presence of abundant pyroxenes shifts the olivine feature toward smaller wavelengths, thus attributing to a fayalite-rich mineral a forsterite-like spectrum. In order to better distinguish the type of the detected olivine, three spectral parameters are used. The first spectral parameter (OSP1 in Table 3) preferentially detects Mg-rich and/or small grain size and/or low abundance olivine. The second spectral parameter (OSP2 in Table 3) is more sensitive to olivine with high iron content and/or large grain size and/or high abundance. An increase of the value of both parameters can be interpreted as an increase of the iron content, and/or of the grain size and/or of the abundance. These two parameters correspond to the two olivine spectral parameters used in *Poulet et al.* [2007], where their thresholds were discussed and tested in detail. In order to better discriminate between olivine with high iron content and/or large grain size and/or a high abundance and Mg-rich and/or small grain size and/or low abundance olivine, we increase the weights applied on the wavelengths 1.36 μm and 1.49 μm as well as the detection threshold of OSP2 to 1.04 instead of 1.02. The third spectral parameter (OSP3 in Table 3) determines the full band depth at 1.36 μm relative to a continuum. It preferentially detects olivine with a large Fe content and/or with large grain size and/or with high abundance. OSP3 is compared to its

median value within a given cube, and only band depths 4% larger than the median are considered as valid detections. This procedure takes advantage of the small fraction of regions exhibiting olivine signatures. It minimizes the impact of aerosol contributions as well as that of departures from linearity of the OMEGA detector (typically 1 to 2%, with variations in behavior from cube to cube).

3.4. Ferric Oxides

[31] The presence of ferric iron absorption features in the UV/visible is indicative of oxidized materials. The degree of oxidation can be evaluated using the strength of the 0.53 μm ferric absorption edge, which is due to several effects: intense Fe^{3+} ligand field transitions between 0.4 and 0.6 μm; Fe^{3+} electronic pair transitions in the 0.5–0.7 μm region; and a strong $O^{2-} \rightarrow Fe^{3+}$ charge transfer absorption centered near 0.25–0.35 μm. To gauge the strength of this feature we use the parameter called BD530, which has been defined by *Morris et al.* [2000] and adapted to OMEGA spectral resolution by *Poulet et al.* [2007].

[32] Ferric phases also exhibit a broad NIR absorption feature centered at 0.86 μm. This feature is indicative of the degree of crystallinity and iron content of the ferric phases. Because of an instrumental artifact around 0.85 μm uncorrected by the previous VIS transfer function, *Poulet et al.* [2007] used the spectral ratio of the reflectance between 0.8 and 0.97 μm to constrain the nature of the ferric oxides. Because of the new visible ITF (Section 2.1), the spectral ratio of the reflectance between 0.78 and 0.88 μm can now be used with confidence to evaluate the 0.86 μm signature. The value of this slope is smaller than unity for ferric oxides with large grain sizes, and becomes larger than unity in presence of nanophase ferric oxide, a few tens of nm or less in size, and increases with the Fe content [*Morris et al.*, 1989]. A value of the 0.88/0.78 μm slope larger than unity can thus be assigned to the presence of nanophase ferric oxides.

[33] Because of the new VIS ITF, values of the Fe^{3+} spectral parameter are systematically lower than those evaluated by *Poulet et al.* [2007]. The nanophase ferric oxide spectral parameter values do not change for the dark regions but are higher for the bright regions.

3.5. Mapping

[34] A resolution of 32 ppd (about 2 km at the equator) was chosen for global mapping because it is well adapted to the spatial sampling of OMEGA observations. Low and middle latitude global maps were built using all observations between $-60°$ and $+60°$, while polar maps were defined for latitudes larger than 50°. For this map resolution of 32 ppd, the OMEGA global coverage reaches about 97% of the Martian surface without applying the MER-based rejection criterion, and 90% with it. The main effect of the presence of aerosols is to decrease the values of all spectral parameters except for the nanophase one. Whenever pixels were observed several times, the best quality data cubes, corresponding to the highest value of each criterion, were used for building the maps, except for the albedo map. For this map, since we do not apply the dust rejection criterion (see section 4.1), we considered all observations of given pixels, then averaged them. This diminishes the effects of atmospheric and surface variations and more homogeneous mosaics are obtained. The low and middle latitudes global maps are plotted over MOLA data in order to emphasize the locations of the detections. The mineralogical south and north polar maps are plotted over the NIR albedo polar maps.

4. Results and Discussion

[35] This section discusses the global maps built on the previously described mineral parameters (Figures 7, 8, and 9).

4.1. NIR Albedo

[36] The NIR albedo map is shown in Figure 7a. To illustrate the global coverage achieved by OMEGA, the MER-based dust rejection criterion is not applied on this albedo map. The average value of albedo for each pixel is mapped. A nearly complete coverage of the Martian surface is obtained, which significantly improves the OMEGA data global coverage of the Martian surface since the 2007 study. The major trends of this map are the same as those of *Poulet et al.* [2007]. The bright regions are localized in the northern hemisphere over the regions of Tharsis, Arabia Terra and Elysium with values ranging from 0.4 to 0.47. In the southern highlands, the regions with the highest albedo are found over the Hellas basin and the region of Promethei. The low NIR albedo regions are mainly localized in the southern hemisphere with the lowest values of $\sim$0.10 in Syrtis Major. Low NIR albedo regions are also identified in the northern hemisphere (the largest one being Acidalia Planitia). All these observations are consistent with previous space and ground-based observations.

4.2. Ferric Oxides

[37] The values of the Fe^{3+} spectral parameter are positive for all the OMEGA pixels, although the degree of oxidation varies significantly. These variations reflect the existence of distinct mineral phases, with different composition and origin. The Fe^{3+} map shows a remarkable spatial correlation with the NIR albedo map (Figures 7a and 7b).

[38] In the dark terrains that exhibit the lowest values of this parameter, the ferric signature could come from ferric-bearing minerals in the pristine rocks, or result from the presence of oxidized phases produced by further weathering or deposition.

[39] The highest Fe^{3+} parameter values of about 0.25 are found in Tharsis. These values are lower than those derived from the 2007 study because of the new visible ITF. Most of the values of the Fe^{3+} spectral parameter in bright regions range from 0.2 to 0.23, in good agreement with values derived from terrestrial analogues of nanophase ferric oxides [*Morris et al.*, 2000].

[40] The regions with large values of the Fe^{3+} parameter are well correlated with those in which the nanophase ferric oxides parameter is larger than 1.0 (Figures 7b and 7c). These observations indicate that the bright regions of Mars are spectrally dominated by nanophase ferric oxides in the VNIR spectral range. This confirms the view that ferric oxides present in the bright Martian regions are in the form of very fine grains. This is also consistent with the low values of the thermal inertia of the three main large areas enriched in nanophase ferric oxides, namely Tharsis, Arabia Terra, and Elysium [e.g., *Mellon et al.*, 2000]. This suggests that the nanophase ferric oxide spectral parameter can be thus interpreted as a dust cover index, which is confirmed by the strong

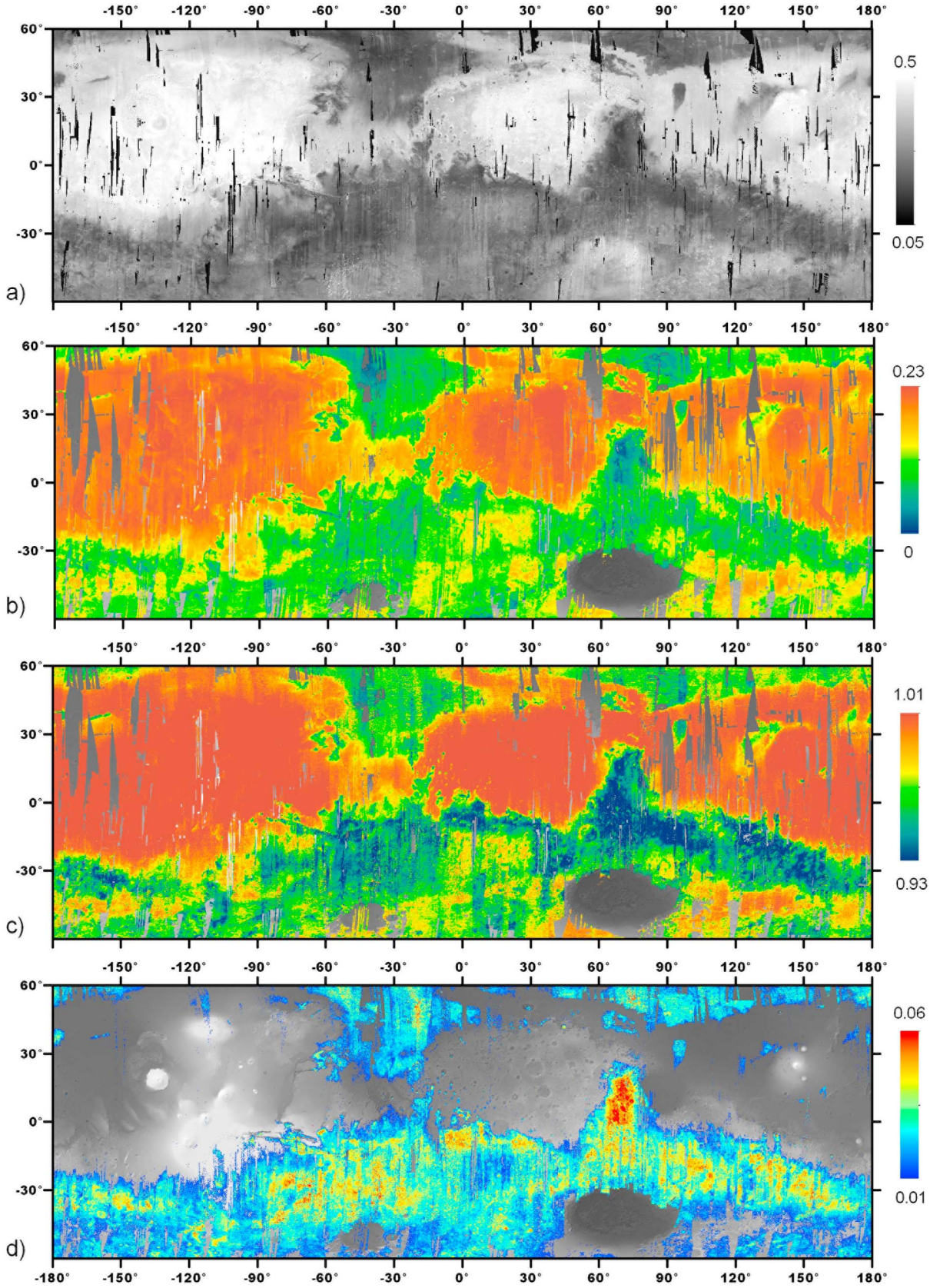

Figure 7. The 32 pixel per degree global spectral parameter maps over MOLA hillshade background: (a) NIR albedo, (b) Fe3+ phase, (c) nanophase ferric oxide, (d) pyroxene. The color scales are indicated for each map. Pixels with values below the detection limit are not plotted.

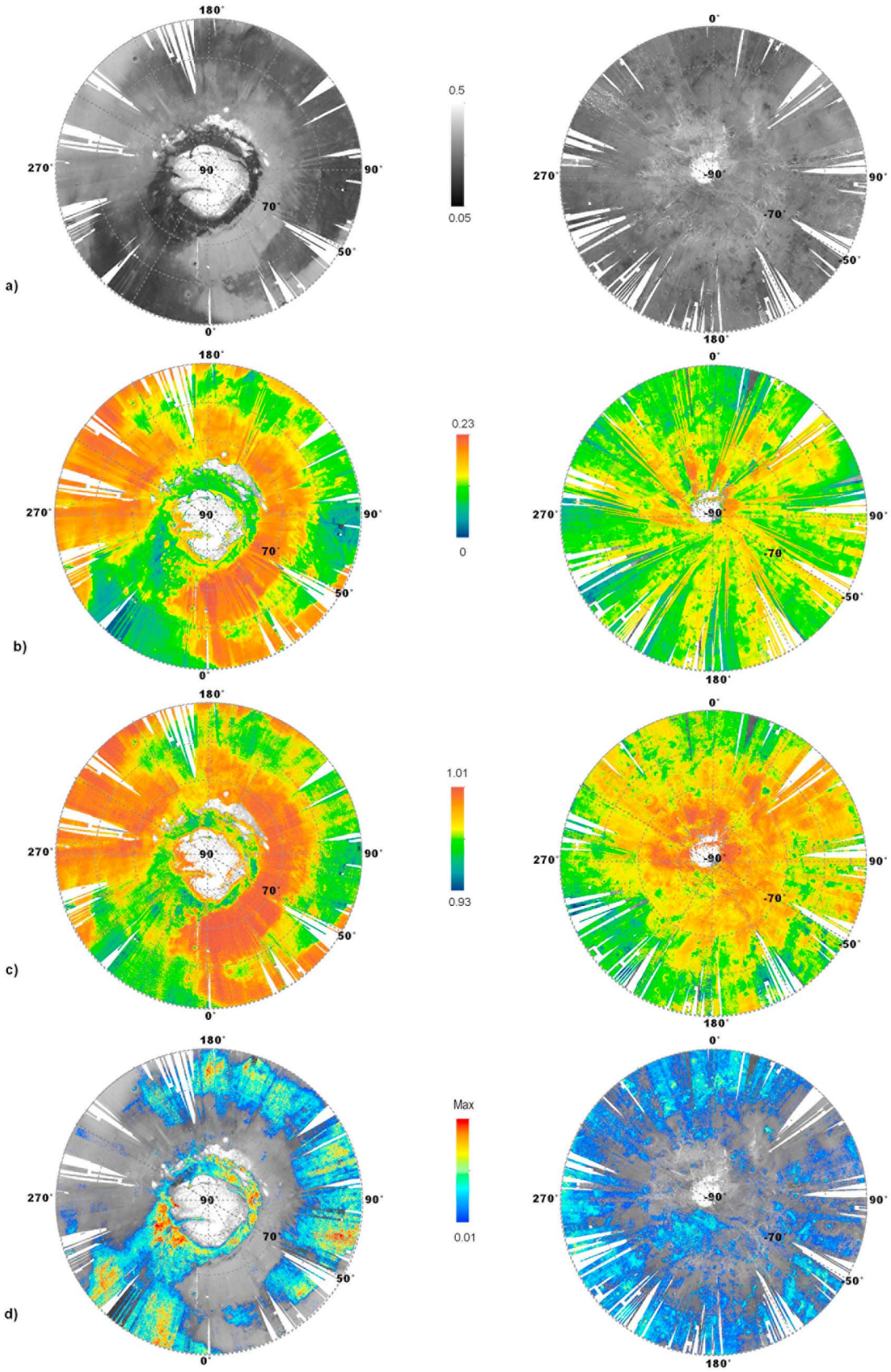

Figure 8

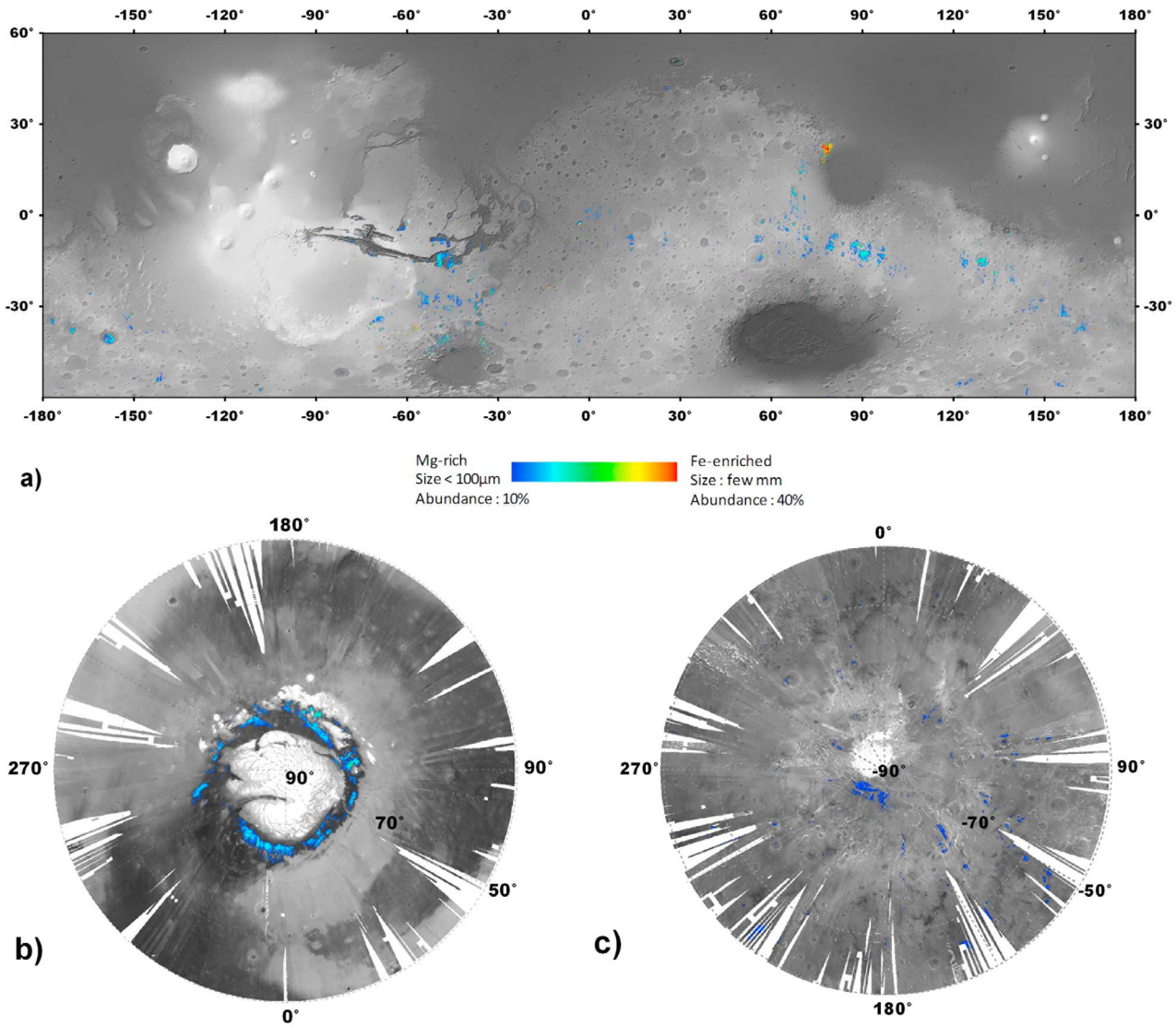

Figure 9. Olivine 32 ppd maps over (a) MOLA map and (b, c) NIR OMEGA albedo map for polar regions. Three olivine spectral parameters are used: detections from blue to green are OSP1values [1.04–1.08]; detections from green to red are OSP2 values [1.04–1.08]; OSP3 values are all mapped in green.

spatial correlation existing between the OMEGA nanophase ferric oxide map and the dust cover index map produced from thermal infrared spectra from the Mars Global Surveyor Thermal Emission Spectrometer (TES) [*Ruff and Christensen*, 2002]. The nanophase ferric oxide map serves as an indicator of surface-obscuring dust that impacts the spectral NIR measurements. Except for very localized terrains, *Poulet et al.* [2005] and *Carter et al.* [2010] report the absence of hydrated minerals over these bright regions, which supports the presence of anhydrous nanophase ferric oxides. Although these regions may exhibit the strongest 3 μm hydration feature [*Jouglet et al.*, 2007; *Milliken et al.*, 2007] and a 6 μm water band [*Ruff*, 2004] interpreted to be the result of the presence of adsorbed water, it has been proposed that the oxides result from an in situ or further weathering processes that do not involve liquid water [*Bibring et al.*, 2006].

[41] Figure 8b shows that the Fe^{3+} spectral parameter is also positive for all OMEGA pixels of the southern and

Figure 8. The 32 pixel per degree spectral parameter (left) North polar map and (right) South polar map over OMEGA albedo background: (a) NIR albedo, (b) Fe3+ phase, (c) nanophase ferric oxide, (d) pyroxene. These polar maps were produced using observations acquired during northern and southern spring and summer, i.e., between Ls = [45°–160°] for the North Pole and Ls = [220°–330°] for South Pole. In order to map both permanent caps, water and CO_2 ices rejection criteria were not applied on NIR albedo polar map between [90°–160°] for the northern polar map and [300°–330°] for the southern polar map. The color scales are indicated for each map; for pyroxene maps, Max corresponds to 0.03 for the North polar map and 0.06 for the South polar map. Pixels with values below the detection limit are not plotted.

northern polar maps, implying that oxidation of the Martian surface is not restricted to low and midlatitudes. The same trend with the albedo is also observed: the higher the albedo, the larger this parameter. As the dust rejection criterion was not applied on polar maps, very strong atmospheric variations in the southern high latitudes interfere with the OMEGA-based mapping of ferric phases, which is evident as radial streaks in the map.

4.3. Pyroxene

[42] The global map of pyroxene presented in Figure 7d is much more complete than that obtained previously [*Poulet et al.*, 2007]. Pyroxene at middle and low latitudes is well correlated with low albedo regions of the ancient highlands with the largest spectral parameter values (5–6%) found in Syrtis Major. This map is consistent with the TES global pyroxene map [*Bandfield*, 2002], although with more detections in the northern lowlands than suggested by the TES map. Pyroxene is also detected in the northern middle and high latitudes low albedo regions as well as in the southern high latitudes but with lower spectral parameter values (2–3%). A large set of articles have been published on the mineralogy of low albedo regions of Mars based on in situ, remote sensing and meteorites observations [e.g., *Bell*, 2008]. It is commonly accepted that the widespread pyroxene-bearing terrains result from volcanic processes, and indicate a mafic igneous composition for the Martian crust.

4.4. Olivine

[43] The olivine global maps (Figure 9) are obtained by using all three olivine spectral parameters (section 3.2.2). The larger data set and new spectral parameters increase by a factor of about 2, the number of olivine detections as compared with OMEGA-based previous mappings. The color range from blue to red is an indicator of the nature of the olivine. Detections mapped in blue correspond to olivine with low iron content and/or with small grain size (less than 100 μm) and/or with a low abundance (about 10%). The color scale bar, from blue to red, can be interpreted in terms of increase of the iron content, increase of the grain size and/or increase in olivine abundance. Thus, detections mapped in red correspond to olivine with high iron content, and/or a large grain size and/or a high abundance (>25%). For example, the best spectral match for the terrains mapped in red in Figure 9a in Nili Fossae was obtained with a grain size of a few mm, a Fe/Mg ratio $\sim$1 and an olivine abundance of 40%. Conversely, a forsteritic composition, with an abundance of about 9% for a grain size of 100 μm was found for the region in Terra Tyrrhena [*Poulet et al.*, 2009b], mapped in blue in Figure 9a. As demonstrated in *Poulet et al.* [2007], given our mapping method and the implementation of a detection threshold, we cannot exclude that low albedo terrains contain small amount (up to 20%) of Mg-rich olivine with small grain size (10 μm or less) mixed with pyroxene and others minerals. We hereafter restrict our discussion to the "olivine-rich" sites, with signatures above thresholds. A detailed analysis of the olivine-bearing terrains is discussed in Ody et al. (submitted manuscript, 2012).

[44] At a global scale, olivine is mostly found associated with low albedo and pyroxene-bearing regions with an uneven distribution. All previously identified olivine regions [*Christensen et al.*, 2000; *Bandfield*, 2002; *Christensen et al.*, 2003; *Hoefen et al.*, 2003; *Hamilton and Christensen*, 2005; *Mustard et al.*, 2005; *McSween et al., 2006*; *Poulet et al.*, 2007; *Koeppen and Hamilton*, 2008, *Edwards et al.*, 2008] including Terra Tyrrhena, Syrtis Major, Eos and Ganges Chasma and detections around the three main basins are detected with our parameters. Numerous additional small deposits, especially around the Argyre and Hellas basins, and extended deposits associated to well define smooth units throughout the southern highlands and in the northern plains have been identified.

[45] These new detections have greatly completed the olivine global map produced by *Poulet et al.* [2007] and have allowed identifying three major geological settings for the olivine-bearing terrains.

[46] 1. Clusters of olivine-rich discontinuous patches on the terraces of the three main basins. Our results strongly suggest that the occurrence of olivine patches around Hellas and Argyre basins is related to the formation of these large basins and represents excavated mantle ejectas. The origin of olivine around the Isidis basin and its unusually large concentration in the Nili Fossae region may have occurred pre-impact [*Hoefen et al.*, 2003; *Hamilton and Christensen*, 2005], contemporaneous [*Mustard et al.*, 2007], or post-impact [*Tornabene et al.*, 2008].

[47] 2. Smooth inter-crater plains and smooth crater floors in the southern highlands. These units are interpreted to result from a resurfacing by olivine-bearing volcanic infillings of various compositions, which could have erupted through local (impact-related) fractures. Olivine is also detected in some crater ejectas, suggesting the presence of olivine-enriched plains, locally buried by a thin coverage of olivine-poor fine particles.

[48] 3. Deposits in the Northern plains. Olivine of various compositions is found in dunes accumulated in crater floors, but also in crater ejectas and extended bedrock exposures. These detections support the idea that a primary olivine-rich basaltic units lies below the sedimentary surface within the northern plains.

[49] These different settings are indicative of a variety of formation processes that are described in detail in Ody et al. (submitted manuscript, 2012).

[50] Regarding to the polar regions, olivine is also detected in the low albedo pyroxene-bearing dunes surrounding the northern polar cap as previously reported in *Poulet et al.* [2008]. This indicates that surface weathering, which could result from the deposition and sublimation of seasonal frosts, is not effective enough to mask the olivine signature. In the southern polar regions, olivine is quasi-absent since only few detections with values close to the detection threshold, have been made.

5. Summary

[51] Based on the full OMEGA data set covering the (0.35 μm–2.6 μm) spectral range, global maps of surface albedo and of key anhydrous surface minerals have been built: ferric oxides, pyroxene and olivine. They result from a new filtering process, which in particular takes into account the atmospheric scattering by aerosols. The spatial distributions are discussed with respect to the geological context in which minerals are detected. The major dichotomy between the ancient magmatic crust, essentially unaltered, and the bright dust that includes nanophase anhydrous ferric oxides,

in addition to feldspars previously detected in the thermal infrared [*Bandfield and Smith*, 2002; *Ruff*, 2004; *Hamilton et al.*, 2005], is confirmed. A variety of olivine-rich spots have been detected, in a few distinct settings within the crust. These maps are stored in ArcGIS format and available upon request. They constitute unique data sets for further global and regional studies.

[52] **Acknowledgments.** We would like to thank Steve Ruff and Rachel Klima for their useful comments and corrections.

References

Bandfield, J. L. (2002), Global mineral distribution on Mars, *J. Geophys. Res.*, *107*(E6), 5042, doi:10.1029/2001JE001510.

Bandfield, J. L., and M. D. Smith (2002), Spectral properties of Martian high albedo regions from MGS-TES, paper presented at AGU, *Eos Trans. AGU*, *83*(19), Spring Meet. Suppl., Abstract P31A-07.

Bell, J., III (2008), *The Martian Surface: Composition, Mineralogy, and Physical Properties*, *Cambridge Planet. Sci.*, vol. 9, edited by J. Bell, Cambridge Univ. Press, Cambridge, U. K., doi:10.1017/CBO9780511536076.

Bellucci, G., F. Altieri, J. P. Bibring, G. Bonello, Y. Langevin, B. Gondet, and F. Poulet (2006), OMEGA/Mars Express: Visual channel performances and data reduction techniques, *Planet. Space Sci.*, *54*, 675–684, doi:10.1016/j.pss.2006.03.006.

Bibring, J.-P., et al. (2004), OMEGA: Observatoire pour la Minéralogie, l'Eau, les Glaces et l'Activité, *Eur. Space Agency Spec. Publ.*, *1240*, 37–49.

Bibring, J.-P., Y. Langevin, J. F. Mustard, F. Poulet, R. Arvidson, A. Gendrin, B. Gondet, N. Mangold, P. Pinet, and F. Forget (2006), Global mineralogical and aqueous Mars history derived from OMEGA/Mars Express data, *Science*, *312*, 400–404, doi:10.1126/science.1122659.

Bonello, G., J. P. Bibring, A. Soufflot, Y. Langevin, B. Gondet, M. Berthé, and C. Carabetian (2005), The ground calibration setup of OMEGA and VIRTIS experiments: Description and performances, *Planet. Space Sci.*, *53*, 711–728, doi:10.1016/j.pss.2005.02.002.

Carter, J., F. Poulet, J.-P. Bibring, and S. Murchie (2010), Detection of hydrated silicates in crustal outcrops in the northern plains of Mars, *Science*, *328*, 1682–1686, doi:10.1126/science.1189013.

Christensen, P. R., J. L. Bandfield, M. D. Smith, V. E. Hamilton, and R. N. Clark (2000), Identification of a basaltic component on the Martian surface from Thermal Emission Spectrometer data, *J. Geophys. Res.*, *105*, 9609–9621, doi:10.1029/1999JE001127.

Christensen, P. R., et al. (2003), Morphology and composition of the surface of Mars: Mars Odyssey THEMIS results, *Science*, *300*, 2056–2061, doi:10.1126/science.1080885.

Edwards, C. S., P. R. Christensen, and V. E. Hamilton (2008), Evidence for extensive olivine-rich basalt bedrock outcrops in Ganges and Eos chasmas, Mars, *J. Geophys. Res.*, *113*, E11003, doi:10.1029/2008JE003091.

Hamilton, V. E., and P. R. Christensen (2005), Evidence for extensive, olivine-rich bedrock on Mars, *Geology*, *33*, 433–436, doi:10.1130/G21258.1.

Hamilton, V. E., H. Y. McSween Jr., and B. Hapke (2005), Mineralogy of Martian atmospheric dust inferred from thermal infrared spectra of aerosols, *J. Geophys. Res.*, *110*, E12006, doi:10.1029/2005JE002501.

Heather, D., N. Manaud, M. Barthelemy, S. Martinez, J. L. Vazquez, and M. Szumlas (2010), The ESA's Planetary Science Archive (PSA), *Eur. Planet. Sci. Congr. Abstr.*, *5*, EPSC2010-46.

Hoefen, T. M., R. N. Clark, J. L. Bandfield, M. D. Smith, J. C. Pearl, and P. R. Christensen (2003), Discovery of olivine in the Nili Fossae region of Mars, *Science*, *302*, 627–630, doi:10.1126/science.1089647.

Jouglet, D., F. Poulet, R. E. Milliken, J. F. Mustard, J.-P. Bibring, Y. Langevin, B. Gondet, and C. Gomez (2007), Hydration state of the Martian surface as seen by Mars Express OMEGA: 1. Analysis of the 3 μm hydration feature, *J. Geophys. Res.*, *112*, E08S06, doi:10.1029/2006JE002846.

Koeppen, W. C., and V. E. Hamilton (2008), Global distribution, composition, and abundance of olivine on the surface of Mars from thermal infrared data, *J. Geophys. Res.*, *113*, E05001, doi:10.1029/2007JE002984.

Langevin, Y., J.-P. Bibring, F. Montmessin, F. Forget, M. Vincendon, S. Douté, F. Poulet, and B. Gondet (2007), Observations of the south seasonal cap of Mars during recession in 2004–2006 by the OMEGA visible/near-infrared imaging spectrometer on board Mars Express, *J. Geophys. Res.*, *112*, E08S12, doi:10.1029/2006JE002841.

Lemmon, M. T., et al. (2004), Atmospheric Imaging Results from the Mars Exploration Rovers: Spirit and Opportunity, *Science*, *306*, 1753–1756, doi:10.1126/science.1104474.

McCord, T. B., R. Clark, and R. L. Huguenin (1982), Mars: Near-infrared reflectance and spectra of surface regions and compositional implications, *J. Geophys. Res.*, *87*, 3021–3032, doi:10.1029/JB087iB04p03021.

McSween, H. Y., et al. (2006), Characterization and petrologic interpretation of olivine-rich basalts at Gusev Crater, Mars, *J. Geophys. Res.*, *111*, E02S10, doi:10.1029/2005JE002477.

Mellon, M. T., T. Michael, B. M. Jakosky, H. H. Kieffer, and P. R. Christensen (2000), High resolution thermal inertia mapping from the Mars Global Surveyor Thermal Emission Spectrometer, *Icarus*, *148*, 437–455, doi:10.1006/icar.2000.6503.

Milliken, R. E., J. F. Mustard, F. Poulet, D. Jouglet, J.-P. Bibring, B. Gondet, and Y. Langevin (2007), Hydration state of the Martian surface as seen by Mars Express OMEGA: 2. H_2O content of the surface, *J. Geophys. Res.*, *112*, E08S07, doi:10.1029/2006JE002853.

Morris, R. V., D. G. Agresti, H. V. Lauer, J. A. Newcomb, T. D. Shelfer, and A. V. Murali (1989), Evidence for pigmentary hematite on Mars based on optical, magnetic, and Mössbauer studies of superparamagnetic (nanocrystalline) hematite, *J. Geophys. Res.*, *94*, 2760–2778, doi:10.1029/JB094iB03p02760.

Morris, R. V., T. D. Shelfer, A. C. Scheinost, N. W. Hinman, G. Furniss, S. A. Mertzman, J. L. Bishop, D. W. Ming, C. C. Allen, and D. T. Britt (2000), Mineralogy, composition, and alteration of Mars Pathfinder rocks and soils: Evidence from multispectral, elemental, and magnetic data on terrestrial analogue, SNC meteorite, and Pathfinder samples, *J. Geophys. Res.*, *105*, 1757–1817, doi:10.1029/1999JE001059.

Mustard, J. F., F. Poulet, A. Gendrin, J.-P. Bibring, Y. Langevin, B. Gondet, N. Mangold, G. Bellucci, and F. Altieri (2005), Olivine and pyroxene diversity in the crust of Mars, *Science*, *307*, 1594–1597, doi:10.1126/science.1109098.

Mustard, J. F., F. Poulet, J. W. Head, N. Mangold, J.-P. Bibring, S. M. Pelkey, C. I. Fassett, Y. Langevin, and G. Neukum (2007), Mineralogy of the Nili Fossae region with OMEGA/Mars Express data: 1. Ancient impact melt in the Isidis Basin and implications for the transition from the Noachian to Hesperian, *J. Geophys. Res.*, *112*, E08S03, doi:10.1029/2006JE002834.

Poulet, F., J.-P. Bibring, J. F. Mustard, A. Gendrin, N. Mangold, Y. Langevin, R. E. Arvidson, B. Gondet, and C. Gomez (2005), Phyllosilicates on Mars and implications for early Martian climate, *Nature*, *438*, 623–627, doi:10.1038/nature04274.

Poulet, F., C. Gomez, J.-P. Bibring, Y. Langevin, B. Gondet, P. Pinet, G. Belluci, and J. Mustard (2007), Martian surface mineralogy from Observatoire pour la Minéralogie, l'Eau, les Glaces et l'Activité on board the Mars Express spacecraft (OMEGA/MEx): Global mineral maps, *J. Geophys. Res.*, *112*, E08S02, doi:10.1029/2006JE002840.

Poulet, F., Y. Langevin, G. Boubin, D. Jouglet, J.-P. Bibring, and B. Gondet (2008), Spectral variability of the Martian high latitude surfaces, *Geophys. Res. Lett.*, *35*, L20201, doi:10.1029/2008GL035450.

Poulet, F., D. W. Beaty, J.-P. Bibring, D. Bish, J. L. Bishop, E. Noe Dobrea, J. F. Mustard, S. Petit, and L. H. Roach (2009a), Key Scientific Questions and Key Investigations from the First International Conference on Martian Phyllosilicate, *Astrobiology*, *9*, 257–267, doi:10.1089/ast.2009.0335.

Poulet, F., et al. (2009b), Quantitative compositional analysis of Martian mafic regions using the MEx/OMEGA reflectance data. 2. Petrological implications, *Icarus*, *201*, 84–101, doi:10.1016/j.icarus.2008.12.042.

Ruff, S. W. (2004), Spectral evidence for zeolite in the dust on Mars, *Icarus*, *168*, 131–143, doi:10.1016/j.icarus.2003.11.003.

Ruff, S. W., and P. R. Christensen (2002), Bright and dark regions on Mars: Particle size and mineralogical characteristics based on Thermal Emission Spectrometer data, *J. Geophys. Res.*, *107*(E12), 5127, doi:10.1029/2001JE001580.

Tornabene, L. L., J. E. Moersch, H. Y. McSween, V. E. Hamilton, J. L. Piatek, and P. R. Christensen (2008), Surface and crater-exposed lithologic units of the Isidis Basin as mapped by coanalysis of THEMIS and TES derived data products, *J. Geophys. Res.*, *113*, E10001, doi:10.1029/2007JE002988.

Vincendon, M., and Y. Langevin (2010), A spherical Monte-Carlo model of aerosols: Validation and first applications to Mars and Titan, *Icarus*, *207*, 923–931, doi:10.1016/j.icarus.2009.12.018.

Vincendon, M., Y. Langevin, F. Poulet, J.-P. Bibring, and B. Gondet (2007), Recovery of surface reflectance spectra and evaluation of the optical depth of aerosols in the near-IR using a Monte Carlo approach: Application to the OMEGA observations of high-latitude regions of Mars, *J. Geophys. Res.*, *112*, E08S13, doi:10.1029/2006JE002845.

Vincendon, M., Y. Langevin, F. Poulet, A. Pommerol, M. Wolff, J.-P. Bibring, B. Gondet, and D. Jouglet (2009), Yearly and seasonal variations of low albedo terrains on Mars in the OMEGA/Mex dataset: Constraints on aerosols properties and dust deposits, *Icarus*, *200*, 395–405, doi:10.1016/j.icarus.2008.12.012.